AGU PUBLICATIONS

JGR

Journal of Geophysical Research: Atmospheres

RESEARCH ARTICLE
10.1002/2016JD026017

Key Points:
- The generation of secondary convection is linked to the downward development of the MCV spawn by the Mei-Yu front MCS
- The descent of the MCV occurs in response to the lowering of the diabatic heating center within the convective system
- Surface cold pool appears to play a minor role in promoting secondary convection, while balanced lifting helps localize the convection

Correspondence to:
M. Xue,
mxue@ou.edu

Citation:
Xu, X., M. Xue, Y. Wang, and H. Huang (2017), Mechanisms of secondary convection within a Mei-Yu frontal mesoscale convective system in eastern China, *J. Geophys. Res. Atmos.*, *122*, 47–64, doi:10.1002/2016JD026017.

Received 2 OCT 2016
Accepted 8 DEC 2016
Accepted article online 12 DEC 2016
Published online 6 JAN 2017

Mechanisms of secondary convection within a Mei-Yu frontal mesoscale convective system in eastern China

Xin Xu[1], Ming Xue[1,2], Yuan Wang[1], and Hao Huang[1]

[1]Key Laboratory of Mesoscale Severe Weather/Ministry of Education and School of Atmospheric Sciences, Nanjing University, Nanjing, China, [2]Center for Analysis and Prediction of Storms and School of Meteorology, University of Oklahoma, Norman, Oklahoma, USA

Abstract The generation of secondary convection, following an earlier episode of convection, within a heavy-rain-producing mesoscale convective system (MCS) along a Mei-Yu front in eastern China on 6–8 July 2013 is studied based on convection-permitting Weather Research and Forecasting simulations. The initiation of the secondary convection is found to be directly linked to the downward development of a mesoscale convective vortex (MCV) spawn by the MCS. In the early and mature stage, the MCV center is located at the middle troposphere; it descends gradually with time as the parent MCS began to decay, with the associated convection transitioning from deep to shallow convection. The descent of the MCV occurs in response to the lowering of the maximum diabatic heating within the convective system, which increases positive potential vorticity down below. When the MCV reaches the lower troposphere, it becomes coupled with the prefrontal southwesterly low-level jet (LLJ). The confluence of the MCV rotational flow with the LLJ notably enhances the convergence on the southern flank of the MCV, where the secondary convection is triggered and swapped through the southeastern flank of the MCV. Unlike that found in the MCV of the U.S. Central Plains, the cold pool produced by the Mei-Yu frontal MCS is rather weak and shallow and appears to play only a minor role in promoting convection. The balanced isentropic lifting by the MCV circulation is also weak, although the MCV circulation does help localize the secondary convection.

1. Introduction

During the summer monsoon season (May to July), a quasi-stationary front commonly forms in the Yangtze-Huaihe River valley in eastern China, which is known as the Mei-Yu front [*Ding and Chan*, 2005]. Different from the midlatitude fronts, the Mei-Yu front features a large moisture gradient but weak thermal contrast and is usually accompanied by a southwesterly low-level jet (LLJ) to its south that transports moisture into the frontal zone [*Ding*, 1992; *Du et al*., 2014]. Mesoscale convective systems (MCSs) often develop and propagate along the Mei-Yu front [*Chen*, 1983; *Chen et al*., 1998; *Qian et al*., 2004]. These Mei-Yu frontal MCSs can sometimes persist several days, producing heavy rain over a large geographical region. For example, a torrential rain-producing MCS was observed on 6–8 July 2013 during the Intensive Observation Period 5 of the Observation, Prediction and Analysis of severe Convection of China Project [*Xue*, 2016] field campaign. This MCS first occurred in central China in the midnight hours (local time) of 6 July (Figure 1a) then moved northeastward along the Mei-Yu front and matured in the early morning of 7 July (Figure 1b). The overall system decayed during the daytime of 7 July but, very interestingly, redeveloped in the evening of 7 July (Figure 1d), producing heavy precipitation of over 100 mm in the coastal areas of Jiangsu province (Figure 2).

The reinvigoration of the MCS is accompanied with the initiation of new convection, which is termed secondary convection in relation to the convection in the early stage [*Trier et al*., 2000b]. Secondary convection can significantly prolong the lifetime of MCSs [e.g., *Fritsch et al*., 1994; *Galarneau et al*., 2009]. According to the warm-season observations in central United States [*Trier et al*., 2000b], secondary convection often initiates near the center of a mesoscale convective vortex (MCV) that develops in the stratiform region of an MCS [*Bartels and Maddox*, 1991]. The interaction between the vertically sheared environment flow and the quasi-balanced MCV can produce isentropic upward (downward) motion in the downshear (upshear) side of the MCV [*Raymond and Jiang*, 1990]. Secondary convection is favored in the downshear side owing to the thermal destabilization of lower troposphere [*Trier et al*., 2000a]. Using the Rapid Update Cycle analyses, *Trier and Davis* [2002] investigated the influence of balanced motion on heavy precipitation within a long-lived MCV. Their results showed that balanced lifting accounted for about half of the total ascent of the unstable air that led to secondary convection. *Trier and Davis* [2007] further studied five MCVs observed in

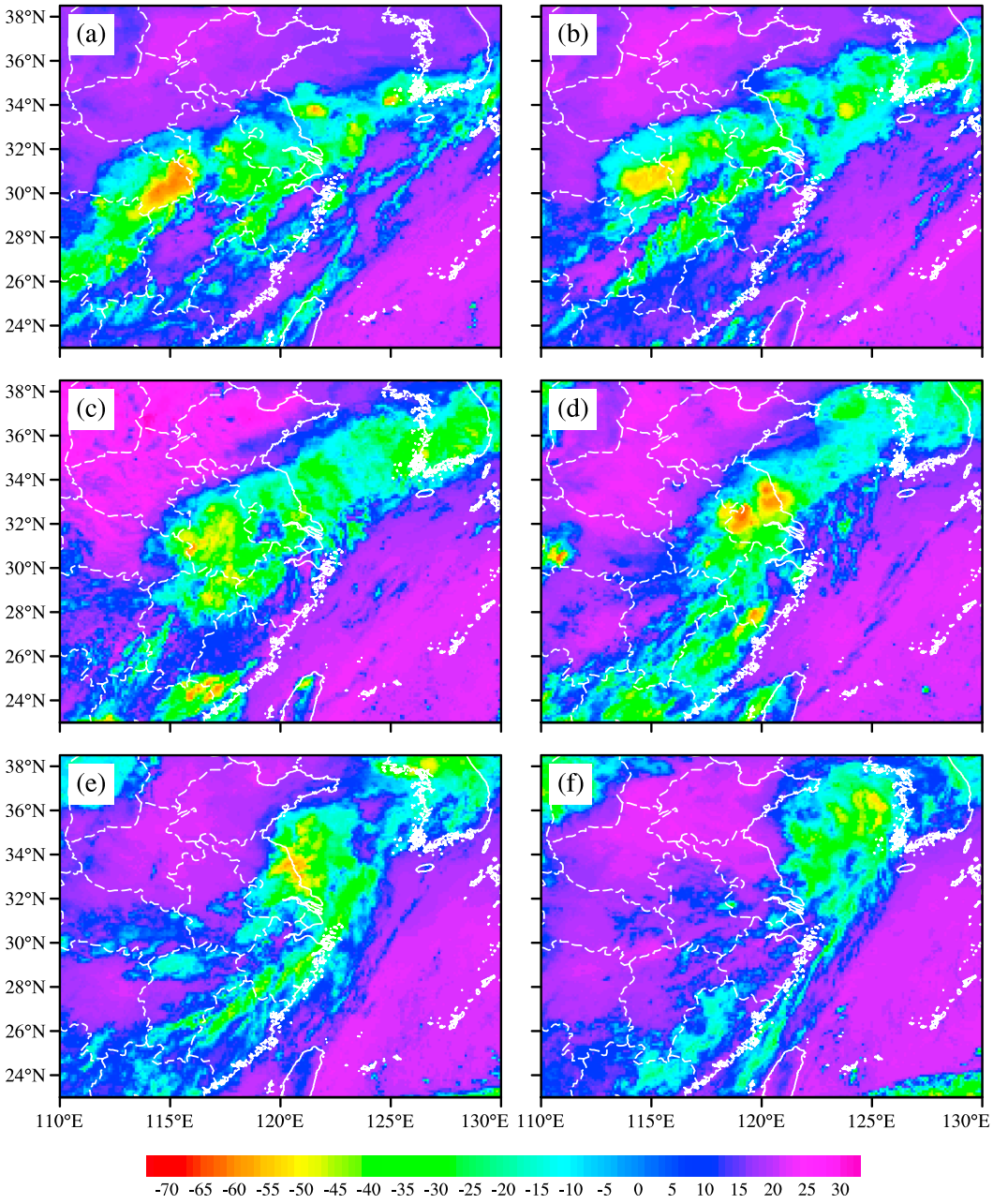

Figure 1. Japan MTSAT-2 satellite infrared image at (a) 1800 UTC 6 July (0200 local standard time 7 July), (b) 0000 UTC 7 July, (c) 0600 UTC 7 July, (d) 1200 UTC 7 July, (e) 1800 UTC 7 July, and (f) 0000 UTC 8 July 2013.

the Bow Echo and Mesoscale Convective Vortex Experiment (BAMEX) [*Davis et al.*, 2004]. Secondary convection was found on the downshear flank of two MCVs that developed in moderate-to-strong vertical shear, accompanied with well-defined mesoscale vertical motion dipole.

In addition to balanced lifting, there are also other mechanisms that help promote secondary convection. *Fritsch et al.* [1994] documented a long-lived, heavy-rain-producing MCV in an environment of weak vertical shear. Secondary convection was repeatedly generated near the vortex center during nighttime, due to the lifting by a surface cold pool beneath the MCV. The relatively fast moving low-level flow ascended to saturation along the upward sloped isentropic surface as it overtook the cold dome. *Trier et al.* [2011] studied the postsunrise reorganization of a nocturnal MCS observed in the International H_2O Project [*Weckwerth et al.*, 2004]. In this case,

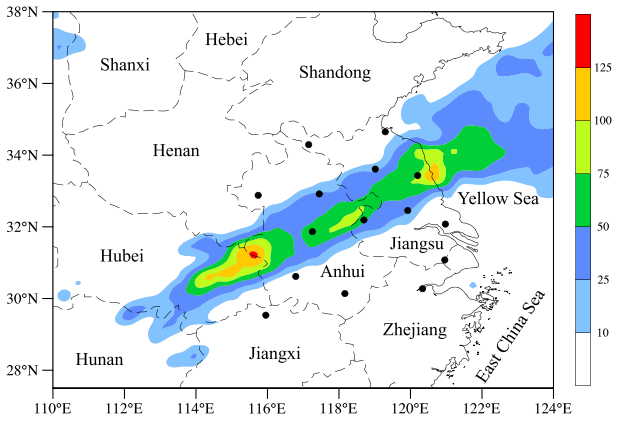

Figure 2. Observation of accumulated precipitation (unit: mm) from 1800 UTC 6 July to 0000 UTC 8 July 2013. Selected provinces and the East China Sea and Yellow Sea are labeled. Black filled circles indicate the radar locations (15 in all).

there was no well-defined surface cold pool; secondary convection was generally fed by conditionally unstable air within an elevated layer resulting from the advection of warm moist air by a LLJ. Moreover, as noted in *Trier et al.* [2006], the ascending branch of cross-frontal circulation can also produce an elevated unstable layer that supports convection reorganization.

Most existing studies focus on the generation of secondary convection associated with warm-season MCSs in central United States. There are relatively few studies on the secondary convection associated with Mei-Yu frontal MCSs. Recently, *Davis and Lee* [2012] performed mesoscale analyses for two heavy rainfall episodes observed in Taiwan during the Southwest Monsoon Experiment and the Terrain-Induced Mesoscale Rainfall Experiment (SoVMEX/TiMREX) [*Jou et al.*, 2011]. Secondary convection was found to occur in phase with the establishment of frontal boundaries near the coast, implying the influence of surface cold pool lifting. *Zhang and Zhang* [2012] and *Luo et al.* [2014] investigated the convective initiation of torrential rain-producing MCSs along the Mei-Yu front in eastern China. Both results suggested the importance of remnant cold pool left behind by previously dissipated convective systems. Deep convection was triggered as the moist monsoonal air ahead of the Mei-Yu front ascended along the upward sloped cold dome. However, no well-defined MCV was reported in these Mei-Yu frontal MCS cases. In this study, we find that the coupling between the convectively generated mesovortex and the prefrontal monsoonal flow can exert a profound influence on the generation of secondary convection.

In this work, the 6–8 July 2013 Mei-Yu frontal MCS in eastern China is studied using a convection-permitting model simulation. Particular interest is paid to the generation of secondary convection during its decaying phase. The primary goal is to seek improved understanding of the reorganization of MCSs within a typical environment of Mei-Yu front in the summer monsoon season of China. The rest of this paper is organized as follows. Section 2 provides an overview of the environment conditions and the evolution of the Mei-Yu front MCS as well as the attendant MCV. Section 3 describes the model configuration of the convection-permitting numerical simulation. Section 4 investigates the generation of secondary convection. The roles of surface cold pool and balanced lifting are also discussed. Finally, this paper is summarized in section 5.

2. Case Overview

The Mei-Yu frontal MCS under consideration developed ahead of a short-wave trough at 500 hPa over central China, stretching from the middle reaches of the Yellow River to the middle-upper Yangtze River valley (Figure 3a). On the other hand, the western Pacific subtropical high (WPSH) was mainly located over the ocean. The southwesterlies between the short-wave trough and the WPSH formed a synoptic LLJ at 850 hPa, extending from south China to Japan (Figure 3b). Cyclonic shear was found on the northern side of the LLJ. The temperature gradient or baroclinicity was very weak in eastern China, which was often observed for Mei-Yu front [*Ding*, 1992]. In its early and mature stage (from 1800 UTC 6 July to 0300 UTC 7 July), the MCS was largely located in eastern Hubei and western Anhui (see map in Figure 2) provinces (Figures 1a, 1b, and 4a). Heavy rainfall of over 125 mm was produced in this area (Figure 2). In the next few hours, the entire system was weakened while propagating northeastward (Figures 1c and 3c). However, secondary convection was generated within the decaying system from about 0900 UTC 7 July (Figures 1d and 1e), which resulted in heavy rain of $>$100 mm near the east coast of Jiangsu province (Figure 2). Close examination of the two precipitation centers revealed that heavy rainfall mainly occurred before (after) 0500 UTC

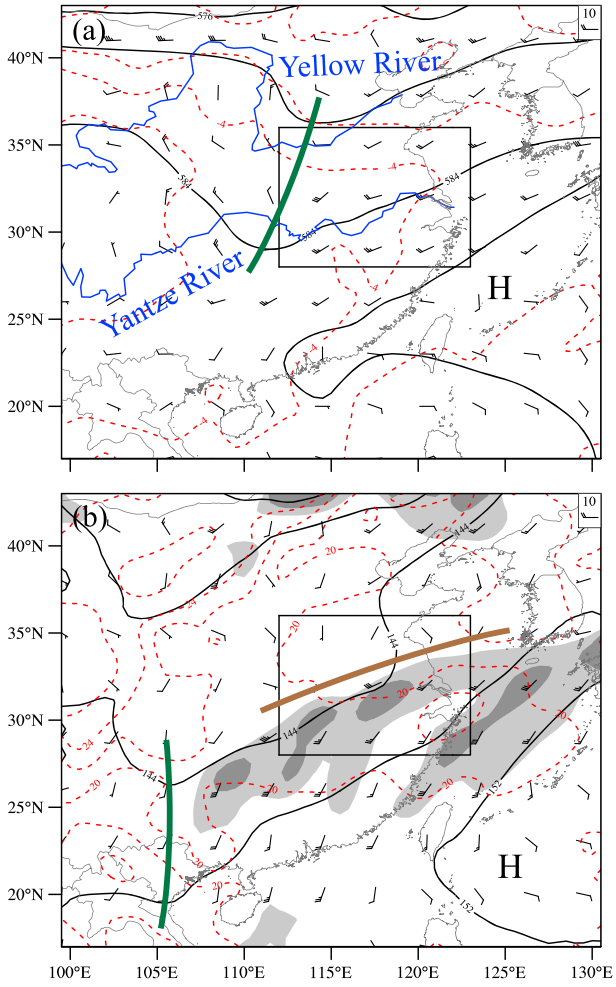

Figure 3. NCEP operational GFS analyses at 1200 UTC 6 July 2013 of geopotential height (contour, unit: 10 gpm), temperature (contour, unit: °C), and wind field at (a) 500 hPa and (b) 850 hPa. Blue lines in Figure 3a denote the Yellow River (north) and the Yangtze River (south). The thick brown line in Figure 3b indicates the shear line, while the thick green line in each panel denotes the short-wave trough. The horizontal wind speed greater than 12 m s^{-1} (15 m s^{-1}) is shaded in light (dark) gray in Figure 3b. The black box indicates the location of the Mei-Yu front MCS of interest.

(1300 UTC) 7 July for the western (eastern) one (not shown). The reorganized MCS eventually arrived in the Yellow Sea and weakened at about 0000 UTC 8 July (Figures 1f and 4e).

Positive vertical vorticity was found in central Anhui province at 0600 UTC 7 July 2013, accompanied with cyclonic circulations (Figure 5a). This is a typical MCV that developed in the stratiform region of an MCS [*Bartels and Maddox*, 1991]. The MCV center was located on the northern end of the leading convective line, which wrapped rearward and formed a well-defined comma head (Figure 4c). Figure 5b depicts the evolution of the mean vertical vorticity near the center of the MCV from 1800 UTC 6 July to 1200 UTC 7 July. In general, there was coherent positive vertical vorticity associated with the MCV from surface to 350 hPa (except at 0000 UTC 7 July). The MCV intensity (in terms of maximum mean vertical vorticity) increased significantly from 1800 UTC 6 July to 0000 UTC 7 July, that is, from the early to mature stage of the MCS. Meanwhile, the level of maximum vertical vorticity shifted upward somewhat from about 800 hPa to 700 hPa. In the mature and decaying stages of the parent MCS, the intensity of the MCV increased slightly, but the level of maximum vorticity decreased from about 650 hPa to a much lower level of 850 hPa. As we will discuss later, the lowering of the MCV is significant for the development of secondary convection.

3. Model Configuration

The 6–8 July 2013 Mei-Yu frontal MCS is simulated using the Advanced Research version of the Weather Research and Forecasting (WRF-ARW) model [*Skamarock et al.*, 2005]. The model is configured with two nested domains. The outer domain has 240 × 220 grids, with a horizontal resolution of 9 km. The inner domain is 1974 × 1796 km^2, and the grid spacing is 3 km (which is considered convection permitting). In the vertical there are 50 levels, with the level interval increasing from about 30 m near the surface to 1300 m at the 50 hPa model top. The physical parameterizations used include the Goddard Space Flight Center microphysics scheme [*Tao et al.*, 1989] based on the *Lin et al.* [1983] scheme, the CAM long-wave and short-wave radiation schemes [*Collins et al.*, 2004], Pleim-Xiu surface layer [*Pleim*, 2006] and land surface model [*Xiu and Pleim*, 2001], and ACM2 planetary boundary layer (PBL) scheme [*Pleim*, 2007]. The PBL scheme also handles the vertical diffusion owing to subgrid-scale turbulent mixing, whereas the horizontal diffusion

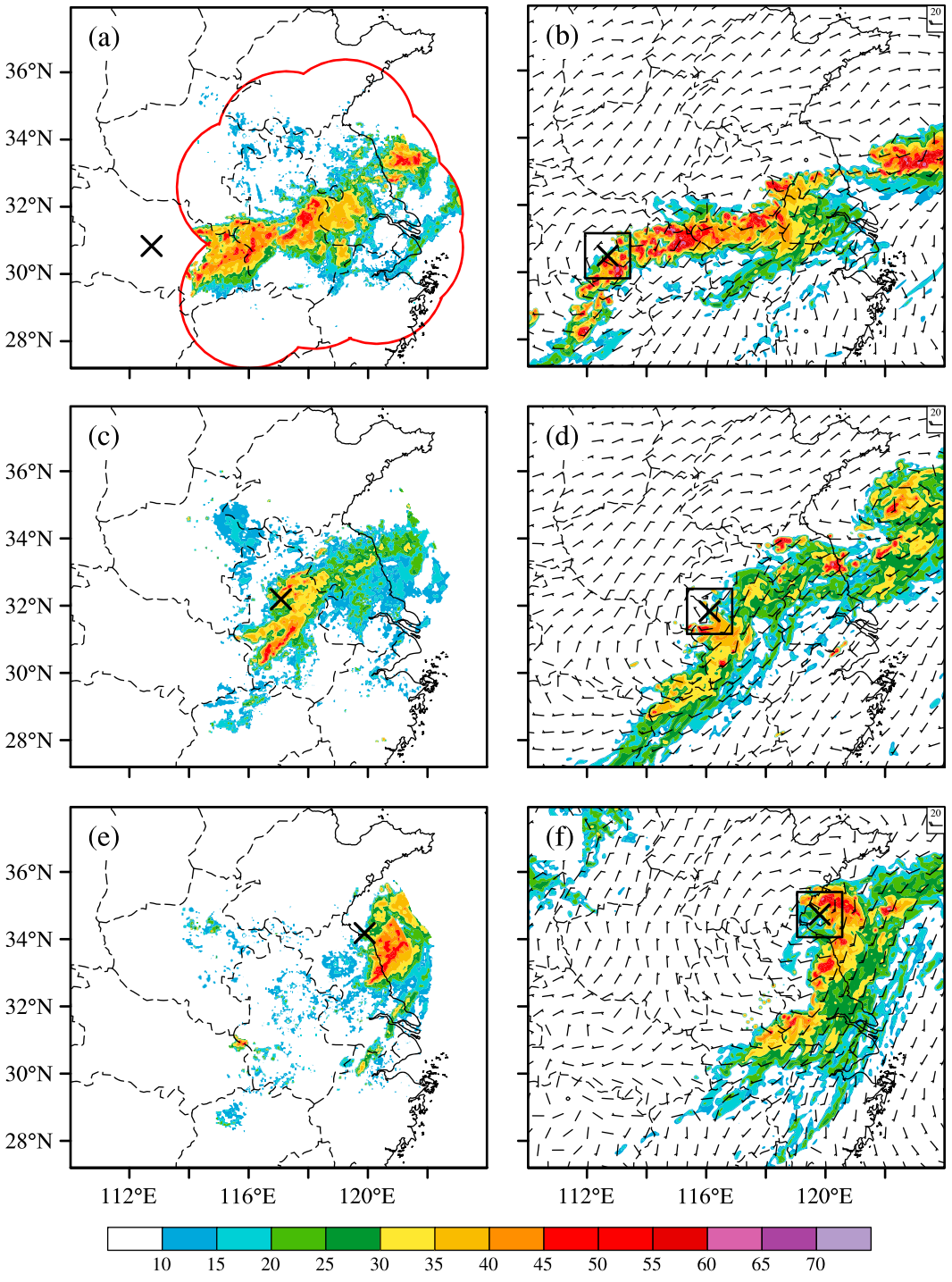

Figure 4. (a, c, and e) Observed and (b, d, and f) simulated composite reflectivity (unit: dBZ) at 1800 UTC 6 July (Figures 4a and 4b), 0600 UTC 7 July (Figures 4c and 4d), and 1800 UTC 7 July 2013 (Figures 4e and 4f). The simulated horizontal wind at 3 km msl is also shown. The black cross marks the position of the MCV center obtained from the GFS analysis and numerical simulation, respectively. (The MCV center is chosen as the location of the maximum vertical vorticity.) The black boxes in Figures 4b, 4d, and 4f are used for area mean within the MCV. The observed reflectivity fields were mosaicked from observations of the 15 radars shown in Figure 2, with the mosaic coverage denoted by the red line in Figure 4a.

is diagnosed from horizontal deformation. Moreover, a 5 km deep sponge layer is placed at the model top to absorb artificial gravity waves; the sixth-order horizontal diffusion [*Xue*, 2000] is employed to damp numerical noise. The model starts at 1200 UTC 6 July 2013, with initial and boundary conditions created from the 6-

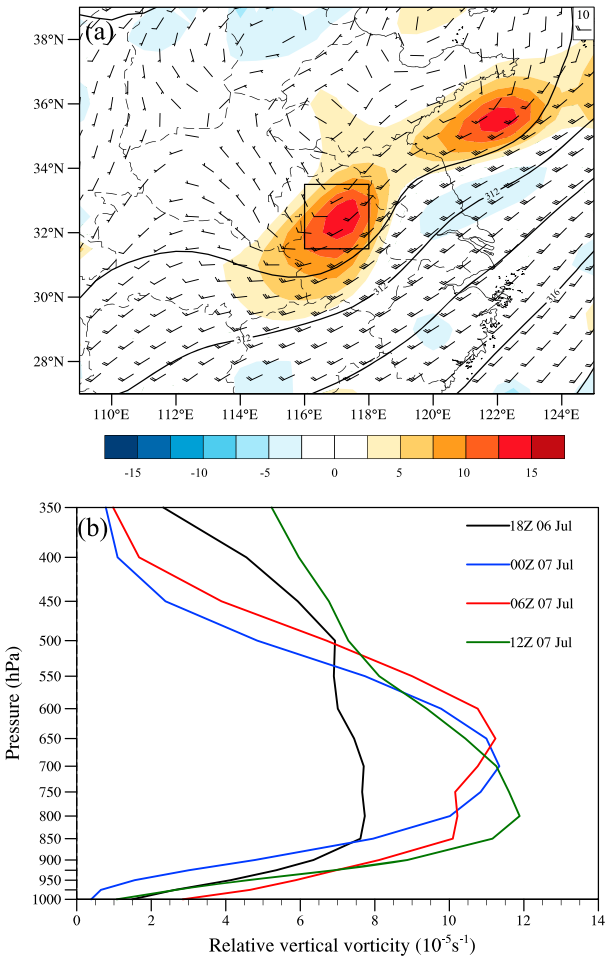

Figure 5. (a) GFS analyses of geopotential height (contour, unit: 10 gpm), wind field, and relative vertical vorticity (shading, unit: 10^{-5} s^{-1}) at 700 hPa 0600 UTC 7 July 2003. (b) Evolution of relative vertical vorticity averaged within a 2° × 2° box at the MCV center (see Figure 5a) following the vortex.

hourly, 0.5° National Centers for Environmental Prediction (NCEP) operational Global Forecast System (GFS) analyses. This experiment is referred to as the control run. As will be shown later, two more sensitivity experiments are also conducted.

4. Results

4.1. Evolution of the Simulated Convective System

At 1800 UTC 6 July, the model produced an elongated convective system in eastern China (Figure 4b). The western part of this convective system was located in northeastern Hunan and central Hubei province, along the southwest-northeast direction. In contrast, the eastern part was mainly west-east oriented, extending from eastern Hubei to western Jiangsu province. Seen from Figure 4a, the eastern convective band was in a reasonably good agreement with the observations. The western portion of the convective line is not seen in the observed reflectivity map in Figure 4a, because of the lack of radar coverage there (see radars used to produce the mosaic in Figure 2). The existence of the western convective band can be inferred from the satellite infrared image (Figure 1a).

At 0600 UTC 7 July, the western convective system evolved into a quasi-linear MCS with a bow shape but weakened in intensity (Figure 4d). In comparison with the observations (Figure 4c) the model MCS was displaced by about 90 km to the southwest. The bow-shaped MCS continued to decay in the next few hours but redeveloped from about 1200 UTC 7 July (i.e., 2–3 h later than observations) associated with the development of secondary convection (see next section). At 1800 UTC 7 July (Figure 4f), the simulated convective system reached the coastal area of Jiangsu province and reorganized into an intense MCS. The northern portion of the MCS was over the ocean such that it was out of the radar detection range (Figure 4e). Nonetheless, the shape of the model MCS was very similar to that observed by satellite (Figure 1e).

The numerical model also reproduced an MCV behind the leading convective line of the MCS (e.g., Figure 4d). This convectively generated meso-β-scale vortex was about 300 to 400 km in diameter, moving in association with the parent MCS. Figure 6 compares the MCV track to its observational counterpart (derived from the GFS analyses). In general, the two tracks agree fairly well with each other. Initially, the simulated MCV was located to the south/west of observations but was biased somewhat to the north after 1200 UTC 7 July. Figure 7 shows the evolution of the average vertical vorticity within the simulated MCV. In the early and mature stages (before 0600 UTC 7 July), the MCV intensity increased rapidly with time, in response to the development of deep convection of the MCS. Meanwhile, the MCV center (the level of maximum vertical vorticity) moved upward from 2.5 km mean sea level (msl) at 1500 UTC 6 July to 3.5 km msl at 0300 UTC 7 July. As the parent MCS decayed from about 0600 UTC 7 July, the MCV intensity showed a slight decrease; on the contrary, the

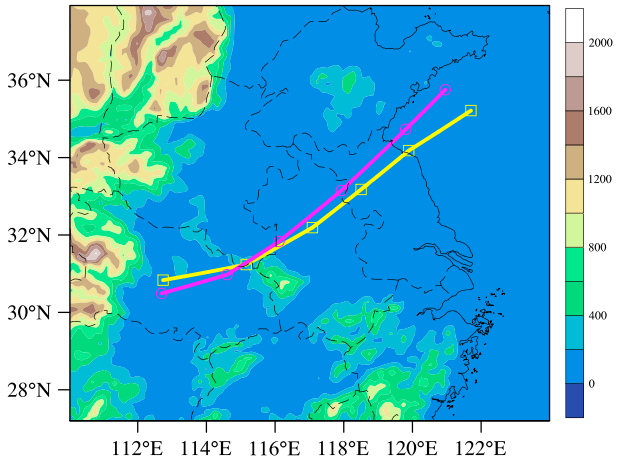

Figure 6. GFS-analyzed (yellow line) and model-simulated (magenta line) tracks of the MCV from 1800 UTC 6 July to 0000 UTC 8 July 2013. The model topography is also shown (shading, unit: meter).

mesovortex center descended significantly with time, reaching a much lower level of about 1.5 km msl at 1200 UTC 7 July. The intensity of MCV began to increase again from 1500 UTC 7 July, as a consequence of new convection developing within the decaying MCS. The downward development of MCV was in a broad agreement with the GFS analysis results presented in section 2.

4.2. Generation of Secondary Convection

Figure 8 shows the composite reflectivity of the simulated MCS between 0800 UTC and 1400 UTC 7 July. Before 1200 UTC 7 July, the overall system became more disorganized due to the continuous weakening of deep convection from 0600 UTC 7 July (Figures 8a–8c). However, there were a few convective cells forming or reintensifying near the MCV center in northeastern Anhui province at 1200 UTC 7 July, namely, the development of secondary convection. (Note that there were also convective cells developing in southern Anhui province in the model, the formation of which was likely attributed to orographic forcing there (see Figure 6).) Two hours later at 1400 UTC 7 July (Figure 8d), the weakening convective system reorganized into an intense, quasi-linear convective system with a comma shape at its northern end.

It is interesting to note that the secondary convection was initiated just as the MCV descended from the middle troposphere to the lower troposphere. The descent of the MCV can significantly enhance the LLJ on its southeastern flank where the ambient flow is in the same direction as the vortex-induced rotational flow. The total wind can be separated into three scales using low-pass, high-pass, and band-pass filters based on discussions of *Barnes* [1973], with the response functions associated with the three scales shown in Figure 9. The small- and large-scale components correspond to horizontal scales of less than 150 km and longer than 2000 km, respectively, whereas the mesoscale component has a peak response function of 90% at 550 km, comparable with the scale of the MCV. The details of the Barnes filters used can be found in Appendix A. Figure 10 presents the results of scale separation for horizontal winds at 1.5 km msl 1200 UTC 7 July. The large-scale winds are predominantly southwesterly along the isobaric line, indicative of geostrophic balance (Figure 10b). A broad LLJ of wind speed greater than 12 m s^{-1} extends northeastward from northern Jiangxi province to the Yellow Sea. At the mesoscale (Figure 10c), there is a low-pressure center in northern Anhui and northwestern Jiangsu province, accompanied by a closed cyclonic circulation (i.e., the MCV). The mesoscale wind exceeds 7 m s^{-1} on the southern and eastern flanks of the MCV, accounting for about 30%–40% of the total wind (Figure 10a). The small-scale wind (Figure 10d) is very weak except in regions of localized convection (see Figure 8c). The enhancement of LLJ by the MCV is qualitatively similar to the generation of high winds caused by low-level mesovortices within quasi-linear convective systems [e.g., *Wakimoto et al*., 2006; *Xu et al*., 2015a]. The intensified LLJ in turn increases the lower tropospheric convergence at its entrance region and its leading edge (nose region). Figure 11 shows the large-scale and mesoscale divergence at 1.5 km msl 1200 UTC 7 July. A broad but weak convergence zone is found in eastern China centered at the southern Anhui province, which is associated with the large-scale southwesterly LLJ (Figure 11a). Conversely, mesoscale convergence occurred in a narrow band extending from southwestern to eastern Anhui province, which is about 1 order of magnitude larger than the large-scale convergence (Figure 11b, note the difference in the color scale from Figure 11a). Subsequently, secondary convection is triggered in the enhanced mesoscale convergence zone.

In order to better understand the origin of parcels that feed into the secondary convection, Lagrangian backward trajectories were calculated for a series of parcels in the area of secondary convection (Figure 12). These

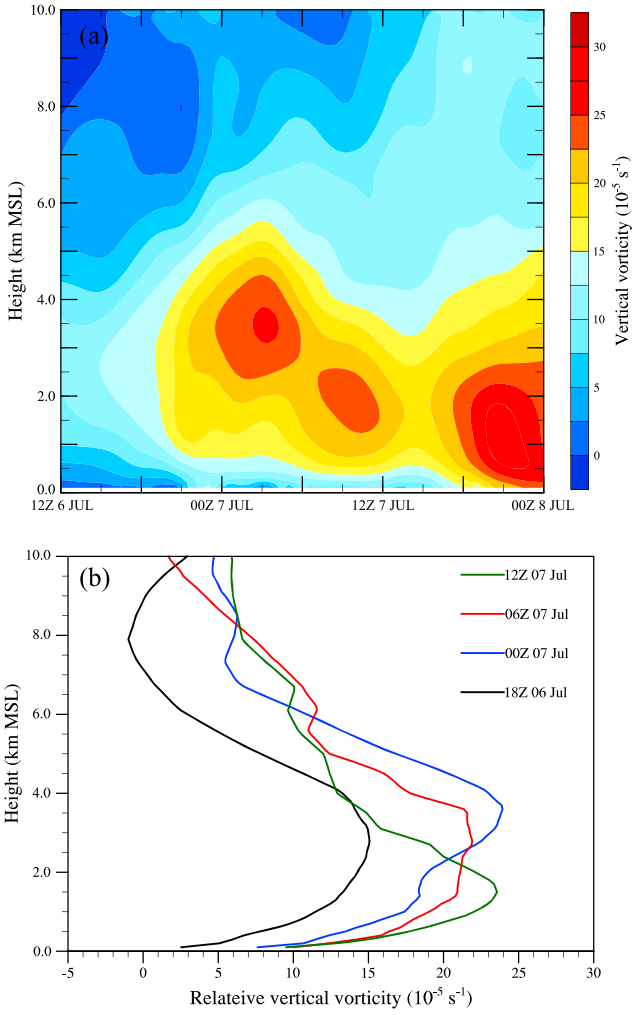

Figure 7. (a) Temporal evolution of the simulated relative vertical vorticity averaged within a 150 × 150 km^2 box between 1200 UTC 6 July and 0000 UTC 8 July 2013. The box is placed at the MCV center, moving with the vortex (see Figure 4). (b) Similar to Figure 5b but for the simulated relative vertical vorticity.

parcels were released at 1.5 km msl 1200 UTC 7 July, integrating backward for 6 h using the model output at 10 min interval. The trajectory was computed using the fourth-order Runge-Kutta scheme. As shown in Figure 12, these parcels had two source regions. The northern parcels came from the western flank of the MCV, which were behind the leading convective line of the MCS at 0600 UTC 7 July (not shown). These parcels were evidently influenced by the vortex rotational flow, showing highly curved trajectories. The southern ones were mainly from ahead of the leading convective line, in association with the southwesterly LLJ. These two sets of air parcels eventually converged on the southeastern flank of the MCV where secondary convection was promoted. The prefrontal monsoonal air has been well recognized as an important ingredient of convective initiation in MCSs along Mei-Yu front [e.g., *Zhang and Zhang*, 2012; *Luo et al*., 2014]. However, the contribution and role of air parcels associated with the MCV vortical flow have not been discussed in these studies. This process was at least qualitatively similar to the juxtaposition of tropical cyclone circulation with southwesterly monsoonal flows, which had been found to be responsible for the production of heavy rainfall within typhoons [*Ge et al*., 2010].

The important role of MCV in promoting the secondary convection is further demonstrated by two additional sensitivity experiments, i.e., NoSML and NoMESO. Unlike the control experiment, these two experiments start at 1200 UTC 7 July 2013 when the simulated MCS in the control run is about to redevelop. Their initial conditions are derived from the control forecast at 1200 UTC 7 July 2013. In NoSML, small-scale disturbances in all fields are removed from the control forecast using the Barnes filters (with the large-scale and mesoscale retained), whereas mesoscale disturbances are removed in NoMESO (details on the Barnes filter are given in Appendix A). Here as in section 4.2, the small- and large-scale components correspond to horizontal scales of less than 150 km and longer than 2000 km, respectively, and the mesoscale component has a peak response function of 90% at 550 km. As a result, structures associated with the weak and disorganized small-scale convection at 1200 UTC are retained (discarded) in experiment NoMESO (NoSML). The large scale is retained in both sensitivity experiments.

Figure 13 displays the forecast composite reflectivity fields at 1400, 1600, and 1800 UTC 7 July for the two sensitivity experiments. In the case of NoMESO, secondary convection did not develop such that the MCS dissipated soon with no reorganization (Figures 13a–13c). In contrast, experiment NoSML succeeded in capturing the general reorganization of the MCS, in a general agreement with the control run and the observations. Deep convection developed on the east/southeast flank of the MCV at 1400 UTC 7 July (Figure 13d), which

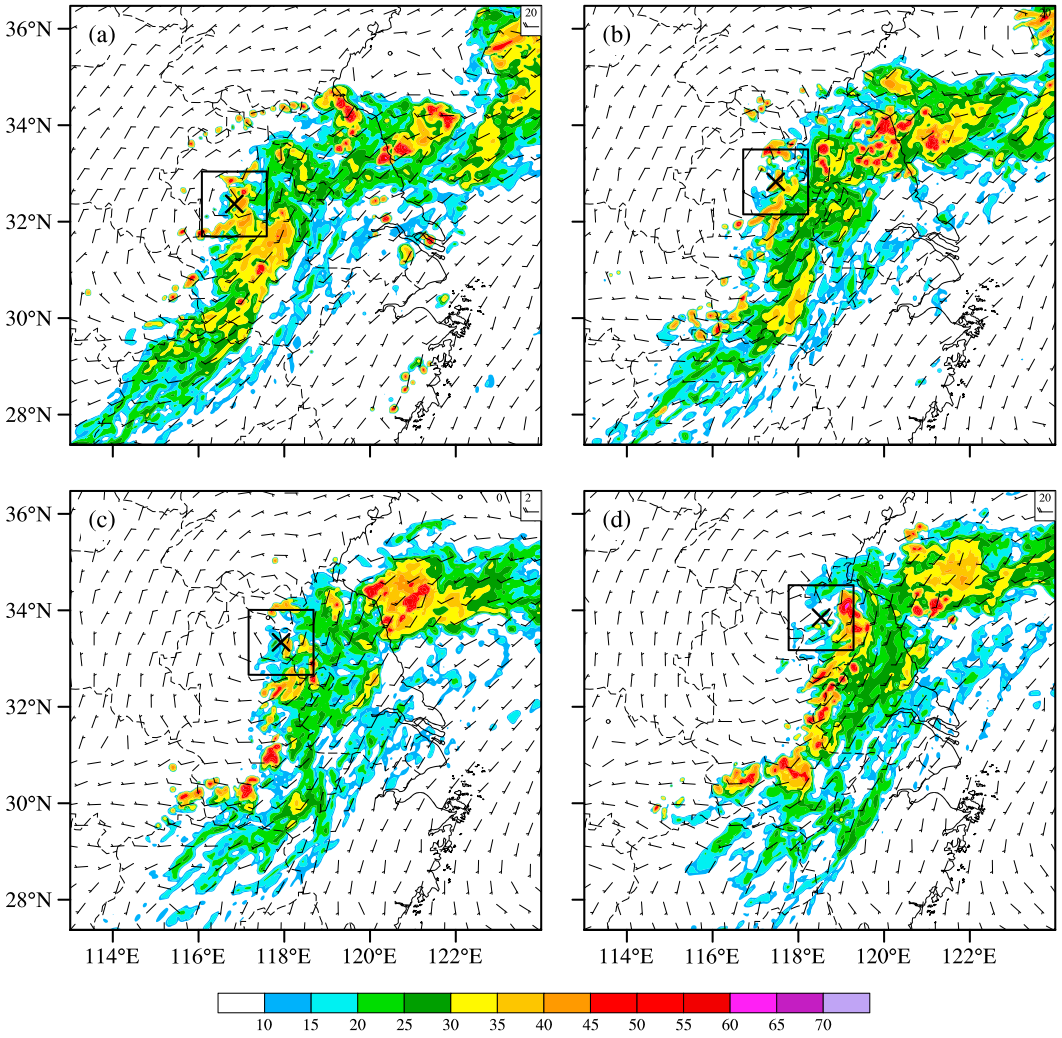

Figure 8. Simulated composite reflectivity at (a) 0800, (b) 1000, (c) 1200, and (d) 1400 UTC 7 July 2013. The horizontal wind at 3 km msl is also shown. The black cross marks the location of the MCV center, whereas the black box is used for area mean calculations within the MCV.

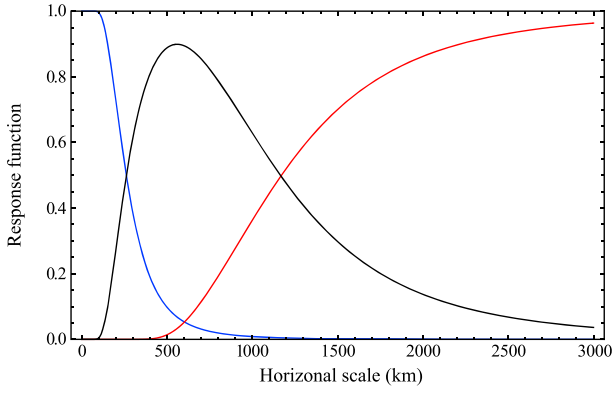

Figure 9. Response function of large-scale (red) low-pass (in terms of wave number), mesoscale band-pass (black) and small-scale (blue) high-pass (for high wave number) filters following *Barnes* [1973].

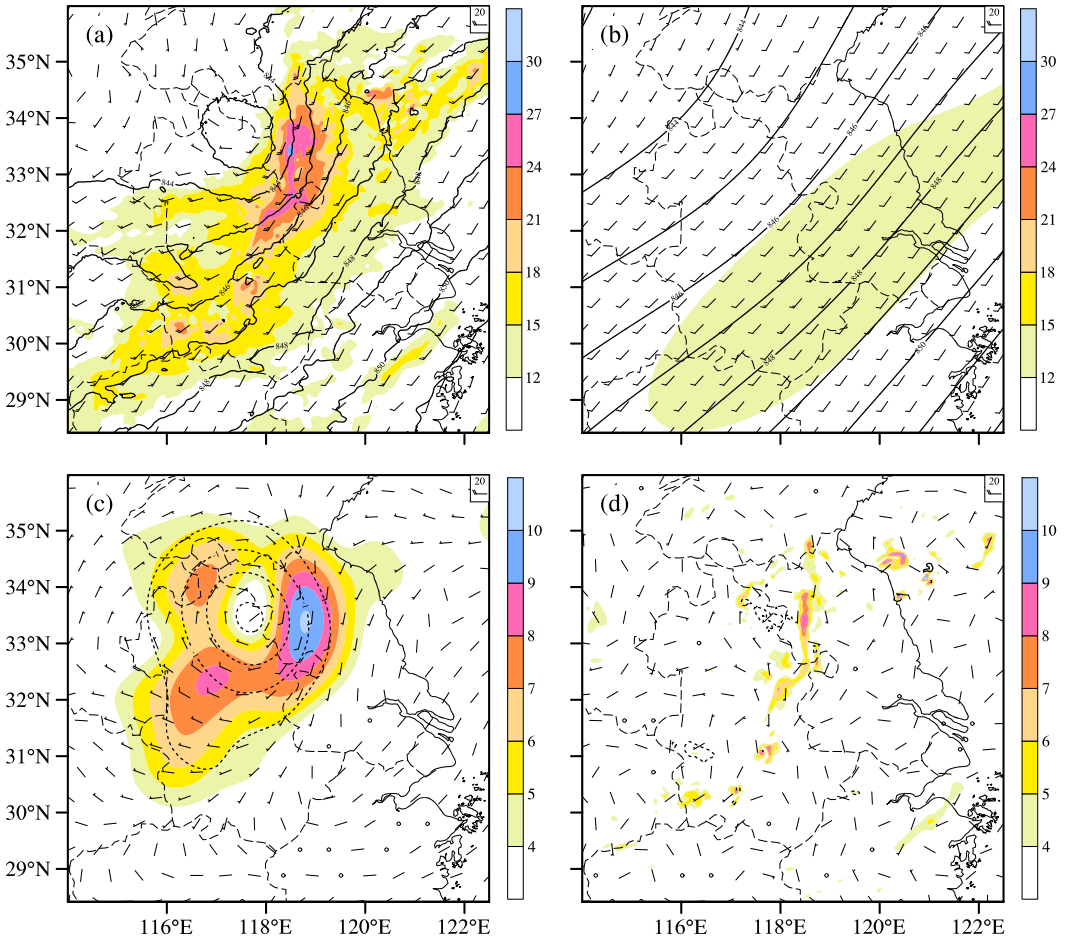

Figure 10. Simulated horizontal wind field and speed (shading, unit: m s^{-1}) and pressure (unit: hPa) at 1.5 km msl 1200 UTC 7 July 2013. (a) The total and decomposed (b) large-scale, (c) mesosacle, and (d) small-scale fields.

organized into an intense convective line in Jiangsu province at 1800 UTC (Figure 13f). Due to the removal of the convection in the initial condition of NoSML, new convection took some time to redevelop, but the broad structure of the MCS is similar to that of control run at 1800 UTC (Figure 4f). These results indicate that the

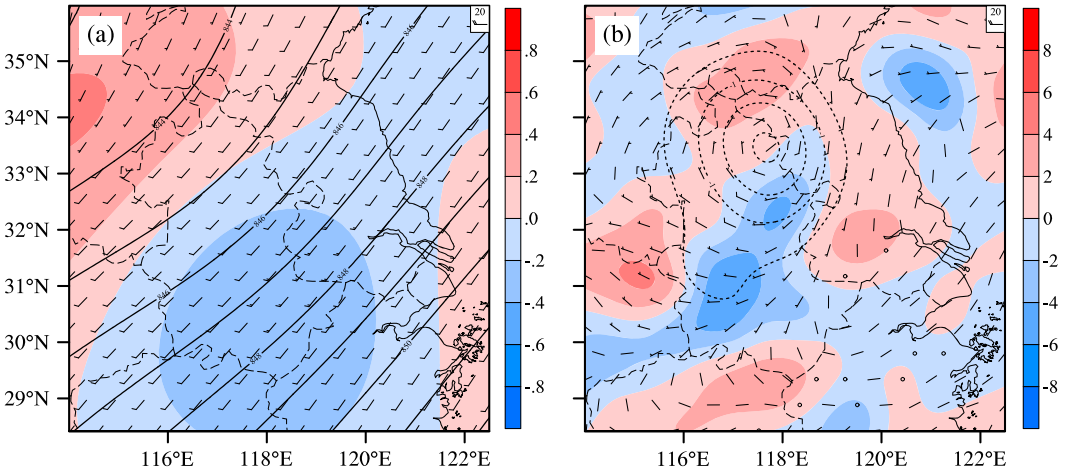

Figure 11. Model-simulated (a) large-scale and (b) mesoscale horizontal divergence (shading, unit: 10^{-5} s^{-1}), horizontal wind, and pressure (contour, unit: hPa) at 1.5 km msl 1200 UTC 7 July 2013.

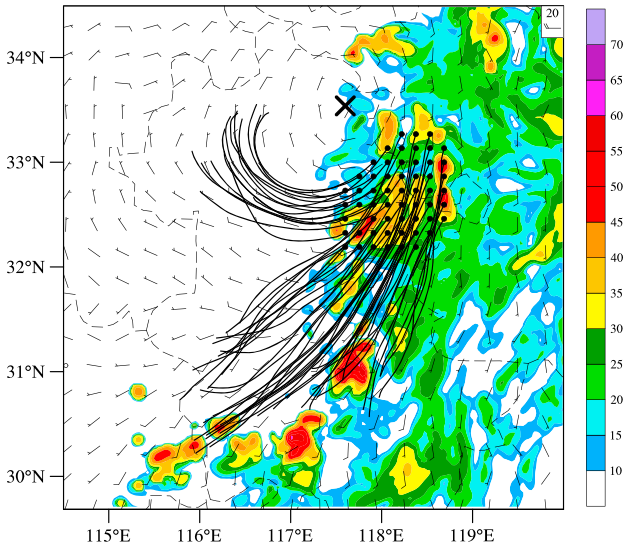

Figure 12. Backward trajectories for air parcels terminating at 1.5 km msl in the region of secondary convection. These parcels are released at 1200 UTC 7 July, integrating backward for 6 h using 10 min model output. The horizontal wind at 1.5 km msl and the MCV center (black cross) are also shown, with the composite reflectivity (unit: dBZ) shaded.

large-scale circulations alone cannot support the secondary convection, and that the MCV plays an important role, which is consistent with the results of *Trier and Davis* [2002], although the exact role played by the MCV in their study is different. In our case, the coupling and interaction between the LLJ and MCV are critical for the generation of secondary convection.

4.3. Physical Interpretation: PV Perspective

Because secondary convection is triggered as the intense MCV descends to the low level and couples with the LLJ, here we study the mechanisms giving rise to the downward development of the MCV. Using WRF simulations at a 4 km grid spacing, *Davis and Galarneau* [2009] addressed the formation, evolution, and vertical structure of two MCVs observed during BAMEX 2003, both of which were accompanied by appreciable cyclonic circulations near the surface. From the viewpoint of vorticity dynamics, the development of low-level vorticity was attributed to the rearward advection of line-end vortex generated along the cold pool outflow boundary (see their Figure 16). While vorticity dynamics can provide insights on the generation of vorticity and/or circulation, the potential vorticity (PV) perspective can also take into account of diabatic heating processes. Here we will discuss the generation of low-level cyclonic circulation from the PV viewpoint, given the presence of significant diabatic processes within the MCS.

The material derivative of PV can be expressed as [e.g., *Raymond and Jiang*, 1990]

$$\frac{Dq}{Dt} = \frac{1}{\rho}\nabla\cdot\left(\dot{H}\boldsymbol{\omega}_a + \theta\nabla\times\mathbf{F}\right), \tag{1}$$

where $q = \frac{1}{\rho}\boldsymbol{\omega}_a\cdot\nabla\theta$ is the Ertel's PV, $\boldsymbol{\omega}_a$ the three-dimensional absolute vorticity, ρ the air density, θ the potential temperature, $\mathbf{F}$ the frictional force, and $\dot{H}$ is the diabatic heating. In the situation of quasi-linear convective systems such as squall lines and bow echoes, the total change of PV is largely dependent on the vertical distribution of diabatic heating [*Hertenstein and Schubert*, 1991]

$$\frac{Dq}{Dt} = \frac{f+\zeta}{\rho}\frac{\partial\dot{H}}{\partial z}, \tag{2}$$

where f is the Coriolis parameter and ζ is the relative vertical vorticity. Under the background of positive absolute vertical vorticity, PV increases (decreases) for positive (negative) vertical gradient of diabatic heating.

Figure 14 shows the area mean diabatic heating profiles within the MCV at 0000 UTC and 0600 UTC 7 July. At the earlier time, which corresponds to the mature phase of the parent MCS, considerable diabatic heating occurred in the middle-upper troposphere, peaking at about 8 km msl, associated with latent heat release within the *deep convection*. Diabatic cooling was found in the low level below about 1 km msl, seemingly due to the evaporation of precipitation. According to equation (2), the most salient creation of PV was in middle troposphere where the vertical gradient of diabatic heating was the greatest. Growth of potential vorticity was also found in the lower troposphere but at a relatively slow rate. At the later time when the parent MCS was decaying, diabatic heating in the middle-upper troposphere was reduced profoundly. The peak heating was lowered to about 3.5 km msl, indicative of shallower convection. While PV still increased in the lower

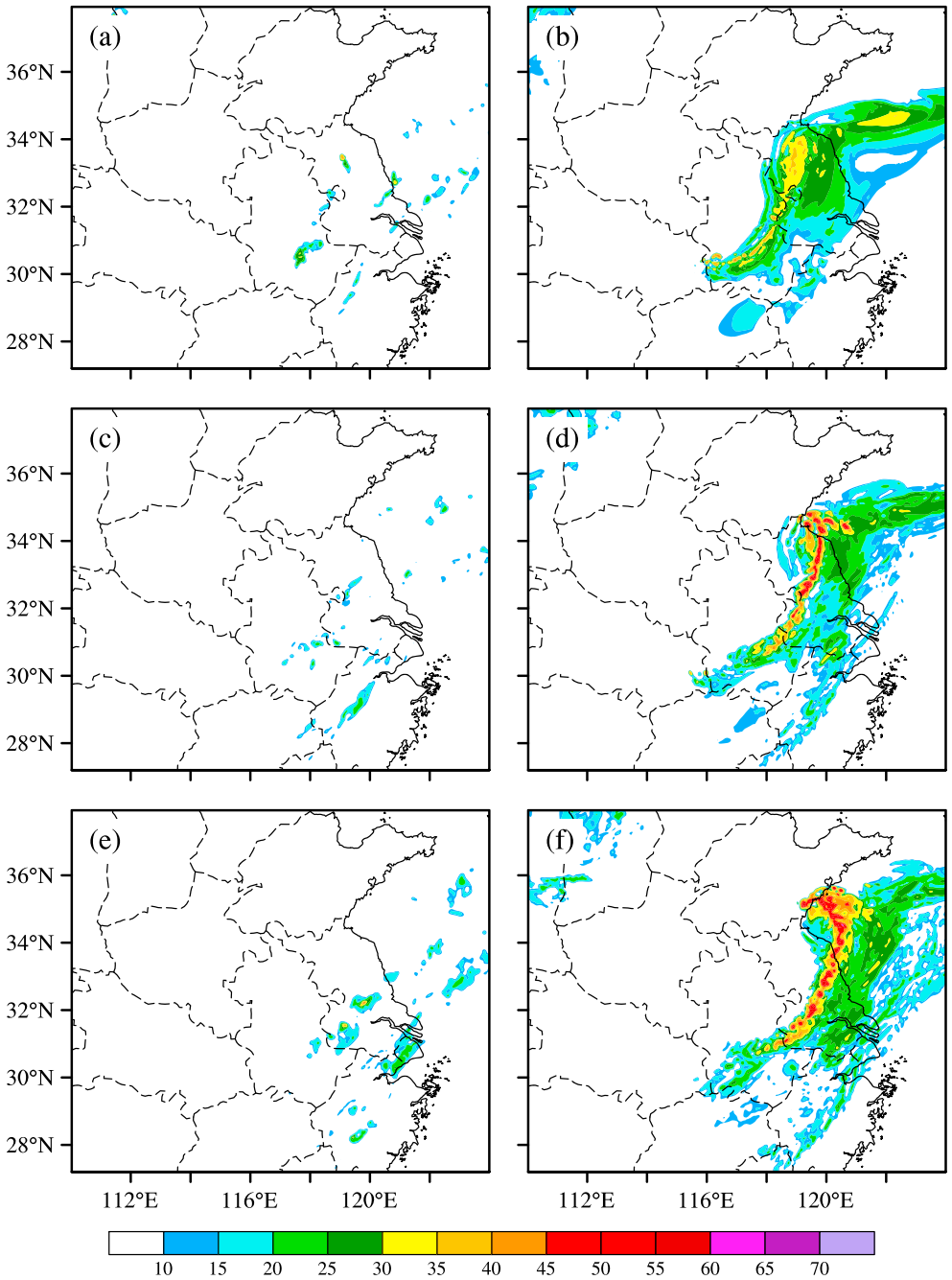

Figure 13. Composite reflectivity at (a) 1400, (c) 1600, and (e) 1800 UTC 7 July 2013 in the NoMESO experiment. (b, d, and f) The same as Figures 13a, 13c, and 13e but for NoSML experiment.

troposphere, it decreased in the middle-upper troposphere. As a result, the convectively generated MCV exhibited a downward development toward the surface.

What caused the changes in the diabatic heating profile then? Figure 15 displays the soundings averaged within the simulated MCV at 1200 UTC 6 July (Figure 15a) and 1200 UTC 7 July (Figure 15b), respectively. Initially, there was approximately 1500 J kg^{-1} of convective available potential energy (CAPE) in the environment. As deep moist convection developed in the early and mature stage of the MCS, the middle-upper atmosphere was heated remarkably while the lower troposphere was chilled (Figure 14). Therefore, the atmosphere became more and more stable with time. The middle-lower troposphere was also moistened due to

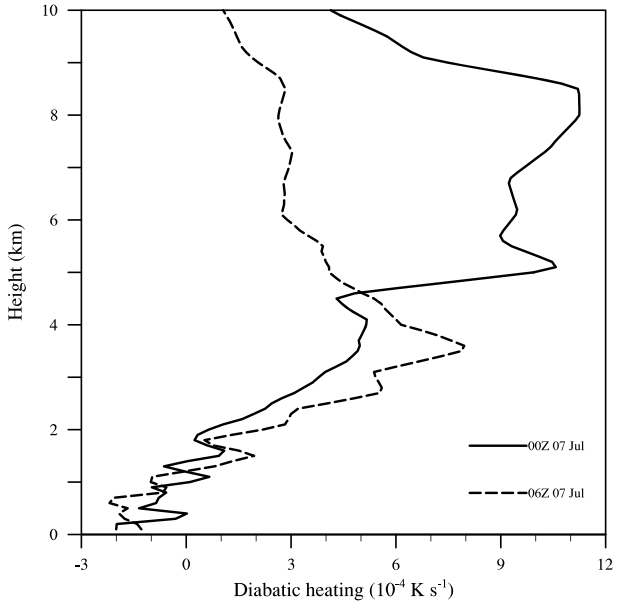

Figure 14. Simulated diabatic heating profiles within the MCV at 0000 (solid) and 0600 (dashed) UTC 7 July 2013. The diabatic heating profiles are averaged within a 150 × 150 km^2 box placed at the MCV center.

the MCS precipitation. In consequence, CAPE decreased to a much lower value of 252 J kg^{-1}. The level of neutral buoyancy descended from about 150 hPa at 1200 UTC 6 July to 400 hPa at 1200 UTC 7 July, implying a transition from deep to shallow convection. This transition can also be inferred from the satellite infrared images. For example, the cloud top was much colder at 1800 UTC 6 July than at 0600 UTC 7 July (Figures 1a and 1c), reflecting a lowering of the cloud top.

The fact that the MCV in this case built downward in an environment of limited thermodynamic instability is similar to the case studied by *Davis and Galarneau* [2009]. Under such a circumstance, the maintenance/development of low-level cyclonic circulation relied heavily on the converging flow at low altitudes to help concentrate the vertical vorticity. In this case, the confluence of the mesovortex rotational flow with the LLJ and the subsequent convection initiated produced such strong convergence. This is in a

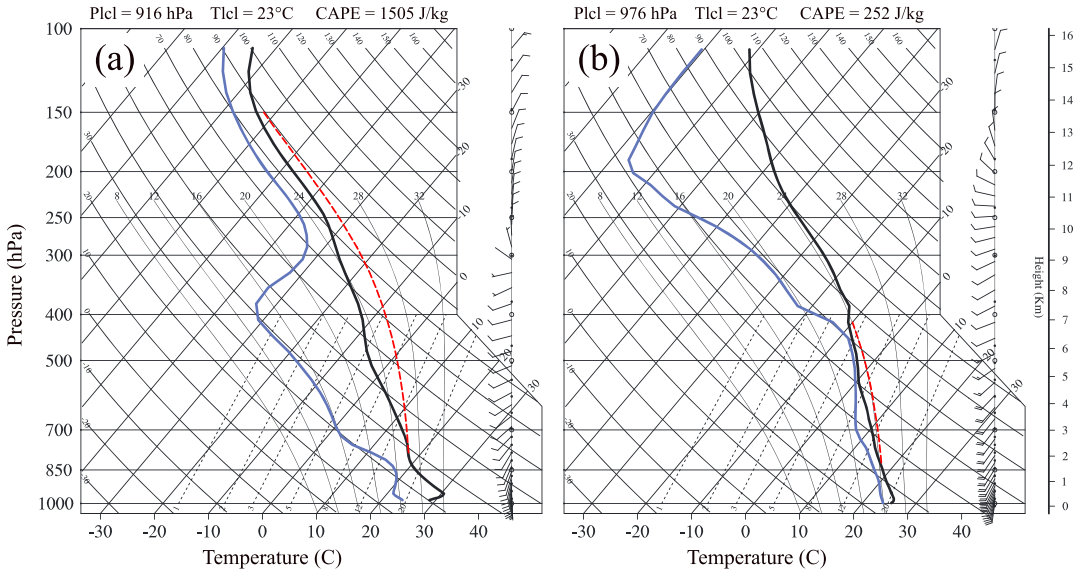

Figure 15. Simulated skew-*T* log-*P* diagram at (a) 1200 UTC 6 July and (b) 1200 UTC 7 July 2013. Both soundings are averaged within a 150 × 150 km^2 box placed at the MCV center.

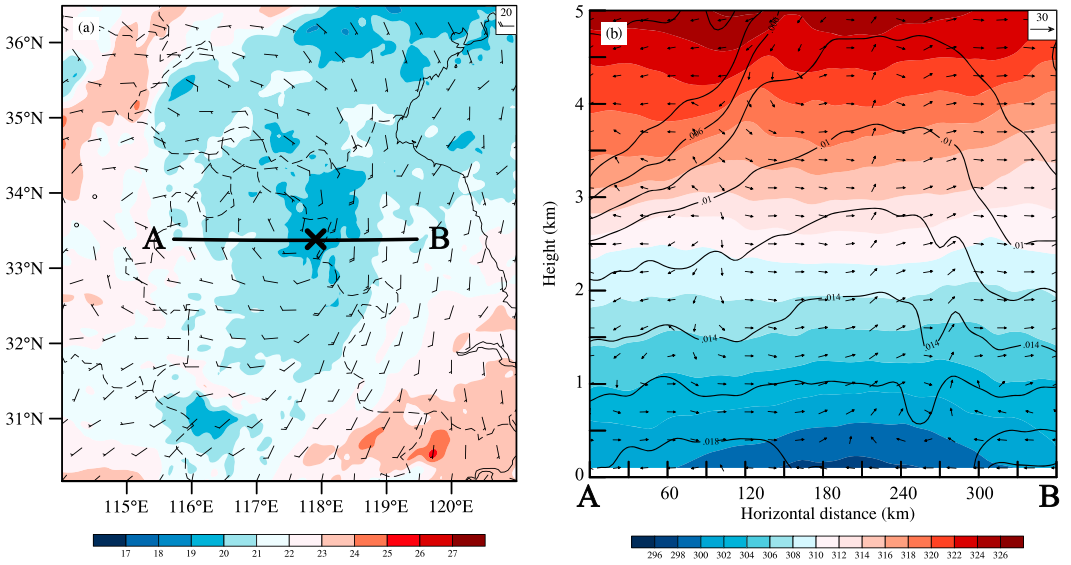

Figure 16. Simulated (a) temperature (shading, unit: °C) and horizontal wind at 1 km msl and (b) potential temperature (shading, unit: K), *u-w* wind, and mixing ratio of water vapor (contour, unit: k kg^{-1}) in the west-east vertical plane AB at 1200 UTC 7 July, from control experiment. Vertical velocity is exaggerated by 10 times in Figure 16b. Black cross in Figure 16 a marks the MCV center.

dynamic analogy to the rapid intensification of low-level mesovortices within a bow echo studied by *Xu et al.* [2015b], in which the enhanced low-level convergence was caused by the descent of the rear inflow jet toward the surface.

4.4. The Roles of Cold Pool and Balanced Isentropic Lifting

Lifting by surface cold pool beneath the MCV has been shown to be helpful in triggering convection in many previous studies [e.g., *Fritsch et al.*, 1994]. New convection will preferentially occur near the MCV center where air parcels can realize the maximum possible ascent along the upward sloped cold dome. However, in the current Mei-Yu frontal MCS case, the cold pool was rather weak, and new convection developed a few tens of kilometers to the south/southeast of the MCV center. As shown in Figure 16a, the vortex center was about 2–3°C colder than the environment at 1 km msl 1200 UTC 7 July. Similarly, small temperature difference was found when examining the cold pool at earlier time (e.g., 0600 UTC 7 July in the mature phase of the MCS, not shown). Moreover, the cold pool was fairly shallow, extending upward to only about 0.5 km msl (Figure 16b).

The production of weak, shallow cold pool can be attributed to the very moist environment in the Mei-Yu season. The East Asia summer monsoon circulation can bring plentiful moisture from the ocean to the Yangtze-Huaihe River valleys in eastern China [*Qian et al.*, 2004]. Moreover, the Mei-Yu front itself is a precipitating system. Precipitation at earlier times can dramatically moisten the atmosphere for the ensuing MCS. Therefore, the evaporation of rainwater is subdued within Mei-Yu frontal MCSs. As shown in Figure 14, there was only weak diabatic cooling below 1 km msl. This is consistent with the mesoscale analyses of two heavy rainfall episodes in Taiwan by *Davis and Lee* [2012]. Shallow frontal boundaries were found near the coast in their cases, which were typically 1 km deep or less, featuring 2–3°C thermal contrasts.

The presence of a weak and shallow cold pool is favorable for the development of MCV at the low levels. *Evans et al.* [2014] studied an intense warm-core MCV associated with the unusually strong 8 May 2009 "Super derecho" event [*Coniglio et al.*, 2011; *Weisman et al.*, 2013; *Xu et al.*, 2015a]. Their results showed that cyclonic circulation increased in the lower troposphere owing to the local expulsion of anticyclonic vorticity within the surface-based cold pool. Similarly, surface cyclogenesis emerged as the midlevel MCV was convectively amplified and overwhelmed the cold high at the surface [*Rogers and Fritsch*, 2001].

Balanced isentropic lifting by an MCV in the presence of vertical environmental shear is another established mechanism for initiating convection in MCV [e.g., *Raymond and Jiang*, 1990]. Secondary convection is favored

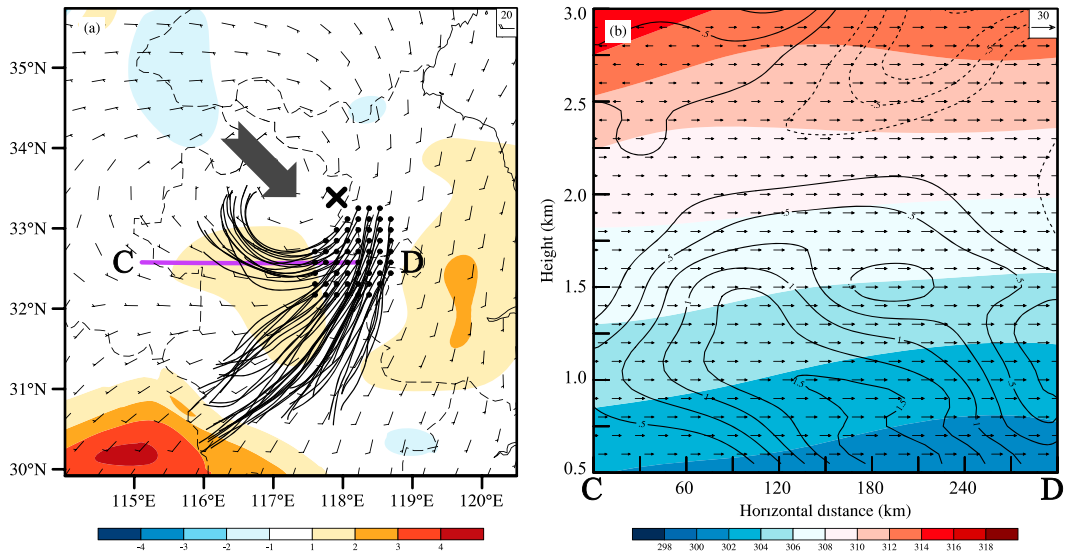

Figure 17. Simulated (a) horizontal wind and isentropic vertical velocity (shading, unit: cm s^{-1}) at 1 km msl and (b) potential temperature (shading, unit: K), *u* component wind, and isentropic vertical velocity (contour, unit: cm s^{-1}) in the west-east vertical plane CD at 1200 UTC 7 July 2013. In Figure 17a, black cross marks the MCV center; thick black arrow denotes the direction of the layer-averaged vertical shear between 0.5 and 1.5 km msl near the MCV. Backward trajectories of parcels terminating at 1.5 km msl within the secondary convection are also shown.

in the downshear side of the MCV where the lower troposphere is thermodynamically destabilized [*Trier et al.*, 2000a]. In this work, the vortex-induced balanced lifting is approximated by the vertical velocity associated with the steady, isentropic, vortex-relative wind $\mathbf{V}_{rel}$, which was termed as isentropic vertical motion (w_I) in *Trier and Davis* [2007],

$$w_I = -\mathbf{V}_{rel}\cdot\nabla_H\theta/(\partial\theta/\partial z). \quad (3)$$

In calculating w_I, we first removed the small-scale disturbances using the Barnes filter, because the balanced motion is largely produced by the mesoscale vortex.

Figure 17a shows the isentropic vertical motion at 1 km msl at 1200 UTC 7 July. The 0.5 to 1.5 km layer-averaged vertical shear is generally southeastward. There is a region of positive $w_I > 1$ cm s^{-1} on the southwestern flank of the MCV (i.e., the downshear right quadrant), while negative $w_I < -1$ cm s^{-1} is found on its northwestern side (i.e., the upshear left quadrant). The magnitude and location of the vertical motion couplet agree with that predicted by the balanced vortex theory [*Raymond and Jiang*, 1990]. Air parcels associated with the vortex rotational flow are more prone to be affected by the balanced lifting, given their remarkable journey through the region of ascending motion. In contrast, some of the parcels from the prefrontal LLJ may miss the vortex-induced uplifting area. Figure 17b displays the isentropic vertical motion in the west-east vertical plane through the trajectories of the northern parcels. Positive w_I is found below ~2 km msl or the level of maximum vortex intensity at this time (see Figure 7). The isentropic vertical motion, in general, decreases with height, with a maximum value less than 2 cm s^{-1}. Given such a small magnitude, the balanced lifting in this case appears to play a minor role in promoting secondary convection. Nevertheless, new convection was generated just downstream of the balanced uplifting region, consistent with *Davis and Trier* [*Trier and Davis*, 2002, Figure 9]. Therefore, balanced lifting may have helped localize the secondary convection.

5. Summary

A heavy-rain-producing MCS was observed along a Mei-Yu front in eastern China on 6–8 July 2013. This long-lived MCS was studied using convection-permitting WRF-ARW simulations, with particular attention paid to the generation of secondary convection in the decaying stage of the MCS. The overall evolution of the MCS was simulated quite well by the numerical model. The composite reflectivity of the MCS in the control simulation was in a good agreement with radar observations, despite some timing and position differences. A convectively generated MCV was spawn by the MCS, which was also reasonably well simulated. More

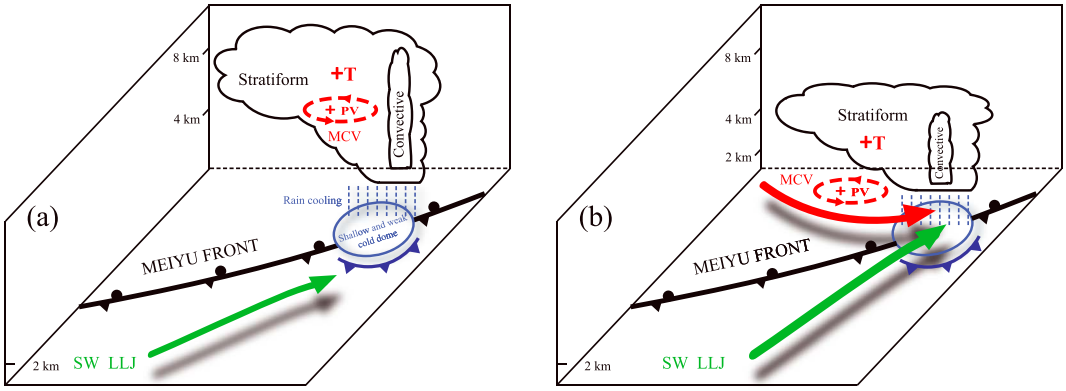

Figure 18. Schematic depicting the generation of secondary convection within Mei-Yu frontal MCS. (a) In the early and mature stage of the MCS, a midtropospheric MCV is developed in the stratiform region behind the leading convective line, featured by positive potential vorticity (PV). A southwesterly low-level jet (LLJ) is present to the south of the Mei-Yu front. Because of the diabatic latent heating (red "+T") in the middle-upper troposphere and evaporative rain cooling in the lower troposphere, the atmosphere becomes more stable over time, no longer supportive of deep convection. (b) In the decaying stage, the MCS is dominated by shallow convection such that the maximum diabatic heating (red +T) is lowered down to the middle-lower troposphere, leading to a downward development of the MCV. Once the meso-β-scale vortex reaches the lower troposphere, it becomes coupled with the prefrontal LLJ. The confluence of the vortex rotational flow with the LLJ can significantly enhance the convergence on the southeastern flank of the MCV where secondary convection is triggered.

importantly, the model succeeded in capturing the generation of secondary convection and thus the redevelopment of the parent MCS.

The initiation of secondary convection was closely related to the downward development of the MCV. In the early and mature stages of the MCS, the MCV center (in terms of maximum vortex intensity) was located at a higher altitude of about 3.5 km msl. As the parent MCS began to decay, the vortex center showed a descending trend with time, reaching a lower level of about 1.5 km msl. This downward building of MCV occurred in response to the temporal change of diabatic heating profile. At the earlier times the MCS was dominated by deep convection. The largest diabatic heating took place in the middle-upper troposphere, whereas the lower atmosphere was cooled by evaporative cooling. This upper heating and bottom cooling jointly increased the stability of the troposphere, giving rise to a pronounced reduction of CAPE with time. In the weakening stage, the MCS was dominated by shallow convection, with the maximum diabatic heating consistently lowered to the middle-lower troposphere. Because positive (negative) PV is created below (above) the level of maximum diabatic heating, the descent of diabatic heating maximum promoted the downward development of the MCV. Once the midlevel meso-β-scale vortex reached the lower troposphere and became coupled with the southwesterly synoptic-scale LLJ, the horizontal convergence was significantly enhanced on its south and southeast flanks where new convection was generated. Backward trajectory analyses clearly revealed that parcels within the secondary convection originated from two distinct source regions. One group of parcels came from the rear of the MCV following highly curved trajectories; that is, these parcels were significantly affected by the vortex circulation. The other group was in association with the prefrontal southwesterly LLJ, whose trajectories were generally from the south. Secondary convection developed when these two sets of parcels converged on the southeastern flank of the MCV. The physical processes described above are summarized in the schematics in Figure 18.

The important role of the MCV in promoting secondary convection was further confirmed by two sensitivity experiments. The results showed that in the absence of the MCV, there was no secondary convection and thus the decaying MCS dissipated quickly. The large and mesoscale circulations alone were enough to cause the development of the secondary convection and therefore reorganization of the MCS even when convective-scale features were removed from the initial condition at a time prior to the secondary convection. The role of surface cold pool lifting was also examined. We found that the cold pool was weak and shallow, extending to only 500 m above ground level. This is not surprising given the very moist environment in the Mei-Yu system, which suppresses evaporative cooling of rain. Therefore, cold pool lifting was believed to

play a minor role in the initiation of secondary convection for our case. Finally, the balanced isentropic lifting by the MCV was also relatively weak, although it might have helped localize the secondary convection. We pointed that more cases will need to be studied to see how representative of the findings of this study is for secondary convection development within Mei-Yu frontal MCVs. The climatological study of secondary convection development within Mei-Yu frontal MCVs should also be carried out.

Appendix A: Details of the Barnes Band-Pass Filter and the Sensitivity Experiments

The Barnes band-pass filter is constructed on the basis of the Barnes objective analysis scheme [*Barnes*, 1973], which aims to generate gridded data $A(x, y)$ from observations A_k, with $k = 1, 2, \ldots, N$ denoting the subscript of observational stations. First, each grid point is assigned a first-guess value

$$A_G(i,j) = \frac{\sum_{k=1}^{k=N} w_k A_k}{\sum_{k=1}^{k=N} w_k A_k}, \tag{A1}$$

where $w_k = \exp\left(-\frac{r_k^2}{4c}\right)$ is the weight function, r_k is the distance between the kth station and the grid (i, j), and c is a prescribed constant. Second, the first-guess field is corrected according to

$$A(i,j) = A_G(i,j) + \frac{\sum_{k=1}^{k=N} w_k' E_k}{\sum_{k=1}^{k=N} w_k' E_k}, \tag{A2}$$

where $E_k = A_k - A_{Gk}$ is the difference (or error) between the observation and first-guess field at the kth station and $w_k' = \exp\left(-\frac{r_k^2}{4c\lambda}\right)$ with $0 < \lambda < 1$. Given the constants λ and c, the response function at wavelength L is

$$R(L) = R_0\left(1 + R_0^{\lambda-1} - R_0^{\lambda}\right), \tag{A3}$$

where $R_0(L) = \exp\left(-\frac{4c\pi^2}{L^2}\right)$ is the response function of formula (A1). The response function given by (A3) represents the percentage of the wave amplitude at horizontal scale L that is retained in the two-pass Barnes objective analysis scheme.

In this study, the model output in the control experiment is considered "observations." Taking the horizontal velocity u as an example, it is first analyzed with $c = 4500$ and $\lambda = 0.3$, producing the small-scale u_s. The corresponding response function is indicated as the blue line in Figure 9, which is a high-pass filter. The remaining u, i.e., $u - u_s$, is then analyzed using $c = 90{,}000$ and $\lambda = 0.3$ to separate the large-scale u_l (see the red line in Figure 9, which is a low-pass filter). Finally, one can obtain the mesoscale u velocity by applying a band-pass filter, namely, $u_m = u - u_s - u_l$.

The band-pass filter is also utilized to generate the initial conditions of the two sensitivity experiments conducted in section 4.2. First, the model output at 1200 UTC 7 July in the control experiment is written in the format of *wrfinput* which is adopted to initialize a new run. Second, this original initial field is modified using the band-pass filter. For experiment NoSML, the small-scale component of each variable stored in *wrfinput* is removed, leaving the large-scale and mesoscale components, i.e., $A_{\text{ini}} = A - A_s = A_l + A_m$. In contrast, the initial condition of experiment NoMESO contains the large-scale and small-scale components; that is, $A_{\text{ini}} = A - A_m = A_l + A_s$. Lastly, the WRF model is run with the modified initial condition at 1200 UTC 7 July.

Acknowledgments

This work was primarily supported by National 973 Fundamental Research Program of China (2013CB430103), National Natural Science Fund of China (41505046), and National Fundamental Research 973 Program of China (2015CB452801). The first author also benefited from discussions with Chris Davis concerning the role of balanced adiabatic lifting. The satellite data are available at http://weather.is.kochi-u.ac.jp/sat/. The GFS analysis can be downloaded freely at http://www.ncdc.noaa.gov/data-access/model-data/model-datasets/global-forcast-system-gfs. The 0.1° gridded precipitation data and the radar observation are provided by the Climatic Data Center at National Meteorological Information Center of China Meteorological Administration, available at https://pan.baidu.com/s/1o8ppil2 (password: 6by5).

References

Barnes, S. L. (1973), Mesoscale objective analysis using weighted time-series observations, NOAA Tech. Memo. ERL NSSL-62, 60 pp. Available from National Severe Storms Laboratory, Norman, OK 73069.

Bartels, D. L., and R. A. Maddox (1991), Midlevel cyclonic vortices generated by mesoscale convective systems, *Mon. Weather Rev.*, *119*(1), 104–118.

Chen, G. T.-J. (1983), Observational aspects of the Mei-Yu phenomena in subtropical China, *J. Meteorol. Soc. Jpn.*, *61*(2), 306–312.

Chen, S.-J., Y.-H. Kuo, W. Wang, Z.-Y. Tao, and B. Cui (1998), A modeling case study of heavy rainstorms along the Mei-Yu front, *Mon. Weather Rev.*, *126*(9), 2330–2351.

Collins, W. D., et al. (2004), Description of the NCAR Community Atmosphere Model (CAM 3.0), *NCAR Tech. Note NCAR/TN–464+STR*, 214 pp., Natl. Cent. for Atmos. Res., Boulder Colo.

Coniglio, M. C., S. F. Corfidi, and J. S. Kain (2011), Environment and early evolution of the 8 May 2009 derecho-producing convective system, *Mon. Wea. Rev.*, *139*, 1083–1102.

Davis, C. A., and T. J. Galarneau Jr. (2009), The vertical structure of mesoscale convective vortices, *J. Atmos. Sci.*, *66*(3), 686–704.

Davis, C. A., and W.-C. Lee (2012), Mesoscale analysis of heavy rainfall episodes from SoWMEX/TiMREX, *J. Atmos. Sci.*, *69*(2), 521–537.

Davis, C. A., et al. (2004), The Bow Echo and MCV Experiment (BAMEX): Observations and opportunities, *Bull. Am. Meteorol. Soc.*, *85*(8), 1075–1093.

Ding, Y.-H. (1992), Summer monsoon rainfalls in China, *J. Meteorol. Soc. Jpn.*, *70*(1), 337–396.

Ding, Y.-H., and J. C. L. Chan (2005), The East Asian summer monsoon: An overview, *Meteor. Atmos. Phys.*, *89*(1), 117–142.

Du, Y., Q. Zhang, Y.-L. Chen, Y. Zhao, and X. Wang (2014), Numerical simulations of spatial distributions and diurnal variations of low-level jets in China during early summer, *J. Clim.*, *27*(15), 5747–5767.
Evans, C., M. L. Weisman, and L. F. Bosart (2014), Development of an intense, warm-core mesoscale vortex associated with the 8 May 2009 "super derecho" convective event, *J. Atmos. Sci.*, *71*, 1218–1240.
Fritsch, J. M., J. D. Murphy, and J. S. Kain (1994), Warm core vortex amplification over land, *J. Atmos. Sci.*, *51*(13), 1780–1807.
Galarneau, T. J., Jr., L. F. Bosart, C. A. Davis, and R. McTaggart-Cowan (2009), Baroclinic transition of a long-lived mesoscale convective vortex, *Mon. Weather Rev.*, *137*(2), 562–584.
Ge, X., T. Li, S. Zhang, and M. Peng (2010), What causes the extremely heavy rainfall in Taiwan during Typhoon Morakot (2009)?, *Atmos. Sci. Lett.*, *11*(1), 46–50.
Hertenstein, R. F. A., and W. H. Schubert (1991), Potential vorticity anomalies associated with squall lines, *Mon. Weather Rev.*, *119*(7), 1663–1672.
Jou, B. J.-D., W.-C. Lee, and R. H. Johnson (2011), An overview of SoWMEX/TiMREX and its operation, in *The Global Monsoon System: Research and Forecast*, 2nd ed., edited by C.-P. Chang, pp. 303–318, World Scientific.
Lin, Y.-L., R. D. Farley, and H. D. Orville (1983), Bulk parameterization of the snow field in a cloud model, *J. Climate Appl. Meteorol.*, *22*(6), 1065–1092.
Luo, Y., Y. Gong, and D.-L. Zhang (2014), Initiation and organizational modes of an extreme-rain-producing mesoscale convective system along a Mei-Yu front in east China, *Mon. Weather Rev.*, *142*(1), 203–221.
Pleim, J. E. (2006), A simple, efficient solution of flux-profile relationships in the atmospheric surface layer, *J. Appl. Meteorol. Climatol.*, *45*(2), 341–347.
Pleim, J. E. (2007), A combined local and nonlocal closure model for the atmospheric boundary layer. Part I: Model description and testing, *J. Appl. Meteorol. Climatol.*, *46*(9), 1383–1395.
Qian, J.-H., W.-K. Tao, and K.-M. Lau (2004), Mechanisms for torrential rain associated with the Mei-Yu development during SCSMEX 1998, *Mon. Weather Rev.*, *132*(1), 3–27.
Raymond, D. J., and H. Jiang (1990), A theory for long-lived mesoscale convective systems, *J. Atmos. Sci.*, *47*(24), 3067–3077.
Rogers, R. F., and J. M. Fritsch (2001), Surface cyclogenesis from convectively driven amplification of midlevel mesoscale convective vortices, *Mon. Wea. Rev.*, *129*, 605–637.
Skamarock, W. C., J. B. Klemp, J. Dudhia, D. O. Gill, D. M. Barker, W. Wang, and J. G. Powers (2005), A description of the Advanced Research WRF version 2, *NCAR Tech. Note NCAR/TN-468+STR*, 88 pp., Natl. Cent. for Atmos. Res., Boulder Colo.
Tao, W.-K., J. Simpson, and M. McCumber (1989), An ice–water saturation adjustment, *Mon. Weather Rev.*, *117*(1), 231–235.
Trier, S. B., and C. A. Davis (2002), Influence of balanced motions on heavy precipitation within a long-lived convectively generated vortex, *Mon. Weather Rev.*, *130*(4), 877–899.
Trier, S. B., and C. A. Davis (2007), Mesoscale convective vortices observed during BAMEX. Part II: Influences on secondary deep convection, *Mon. Weather Rev.*, *135*(6), 2051–2075.
Trier, S. B., C. A. Davis, and W. C. Skamarock (2000a), Long-lived meso-convective vortices and their environment. Part II: Induced thermodynamic destabilization in idealized simulations, *Mon. Weather Rev.*, *128*(10), 3396–3412.
Trier, S. B., C. A. Davis, and J. D. Tuttle (2000b), Long-lived meso-convective vortices and their environment. Part I: Observations from the central United States during the 1998 warm season, *Mon. Weather Rev.*, *128*(10), 3376–3395.
Trier, S. B., C. A. Davis, D. A. Ahijevych, M. L. Weisman, and G. H. Bryan (2006), Mechanisms supporting long-lived episodes of propagating nocturnal convection within a 7-day WRF model simulation, *J. Atmos. Sci.*, *63*(10), 2437–2461.
Trier, S. B., J. H. Marsham, C. A. Davis, and D. A. Ahijevych (2011), Numerical simulations of the postsunrise reorganization of a nocturnal mesoscale convective system during 13 June IHOP_2002, *J. Atmos. Sci.*, *68*(12), 2988–3011.
Wakimoto, R. M., H. V. Murphey, C. A. Davis, and N. T. Atkins (2006), High winds generated by bow echoes. Part II: The relationship between the mesovortices and damaging straight-line winds, *Mon. Weather Rev.*, *134*(10), 2813–2829.
Weckwerth, T. M., D. B. Parsons, S. E. Koch, J. A. Moore, M. A. Lemone, B. B. Demoz, C. Flamant, B. Geerts, J. Wang, and W. F. Feltz (2004), An overview of the International H2O Project (IHOP_2002) and some preliminary highlights, *Bull. Am. Meteorol. Soc.*, *85*(2), 253–277.
Weisman, M. L., C. Evans, and L. Bosart (2013), The 8 May 2009 superderecho: Analysis of a real-time explicit convective forecast, *Wea. Forecasting*, *28*, 863–892.
Xiu, A., and J. E. Pleim (2001), Development of a land surface model. Part I: Application in a mesoscale meteorological model, *J. Appl. Meteorol.*, *40*(2), 192–209.
Xu, X., M. Xue, and Y. Wang (2015a), Mesovortices within the 8 May 2009 bow echo over Central US: Analyses of the characteristics and evolution based on Doppler radar observations and a high-resolution model simulation, *Mon. Weather Rev.*, *143*(6), 2266–2290.
Xu, X., M. Xue, and Y. Wang (2015b), The genesis of mesovortices within a real-data simulation of a bow echo system, *J. Atmos. Sci.*, *72*(5), 1963–1986.
Xue, M. (2000), High-order monotonic numerical diffusion and smoothing, *Mon. Weather Rev.*, *128*(8), 2853–2864.
Xue, M. (2016), Preface to the special issue on the "Observation, Prediction and Analysis of severe Convection of China" (OPACC) National "973" Project, *Adv. Atmos. Sci.*, *33*(10), 1099–1101.
Zhang, M., and D.-L. Zhang (2012), Subkilometer simulation of a torrential-rain-producing mesoscale convective system in east China. Part I: Model verification and convective organization, *Mon. Weather Rev.*, *140*(1), 184–201.